Available online at www.sciencedirect.com
ScienceDirect
Bioorganic & Medicinal Chemistry 16 (2008) 6103–6115
Bioorganic & Medicinal Chemistry

Structural requirements of pyrido[2,3-*d*]pyrimidin-7-one as CDK4/D inhibitors: 2D autocorrelation, CoMFA and CoMSIA analyses

Julio Caballero,[a,*] Michael Fernández[b,c] and Fernando D. González-Nilo[a]

[a]*Centro de Bioinformática y Simulación Molecular, Universidad de Talca, 2 Norte 685, Casilla 721, Talca, Chile*
[b]*Molecular Modeling Group, Center for Biotechnological Studies, University of Matanzas, Matanzas, Cuba*
[c]*Department of Bioscience and Bioinformatics, Kyushu Institute of Technology (KIT), 680-4 Kawazu, Iizuka, Fukuoka 820-8502, Japan*

Received 12 March 2008; revised 16 April 2008; accepted 17 April 2008
Available online 25 April 2008

Abstract—2D autocorrelation, comparative molecular field analysis (CoMFA) and comparative molecular similarity indices analysis (CoMSIA) were undertaken for a series of pyrido[2,3-*d*]pyrimidin-7-ones to correlate cyclin-dependent kinase (CDK) cyclin D/CDK4 inhibition with 2D and 3D structural properties of 60 known compounds. QSAR models with considerable internal as well as external predictive ability were obtained. The relevant 2D autocorrelation descriptors for modeling CDK4/D inhibitory activity were selected by linear and nonlinear genetic algorithms (GAs) using multiple linear regression (MLR) and Bayesian-regularized genetic neural network (BRGNN) approaches, respectively. Both models showed good predictive statistics; but BRGNN model enables better external predictions. A weight-based input ranking scheme and Kohonen self-organized maps (SOMs) were carried out to interpret the final net weights. The 2D autocorrelation space brings different descriptors for CDK4/D inhibition, and suggests the atomic properties relevant for the inhibitors to interact with CDK4/D active site. CoMFA and CoMSIA analyses were developed with a focus on interpretative ability using coefficient contour maps. CoMSIA produced significantly better results. The results indicate a strong correlation between the inhibitory activity of the modeled compounds and the electrostatic and hydrophobic fields around them.

1. Introduction

Cyclin-dependent kinases (CDKs) are a family of serine–threonine kinases that play important roles as regulators of cell progression through consecutive phases of the cell cycle.[1] CDKs are regulated by phosphorylation and activated by their association with cyclins.[2] The precise regulation of CDK activity is essential for the stepwise execution of the many processes required for cell growth and division, including DNA replication and chromosome separation.[3] Abnormal CDK control of the cell cycle has been strongly linked to the molecular pathology of cancer.[4] Such revelations have led to the investigation of small molecule CDK inhibitors (CDKIs) as possible cancer therapeutics.[5,6]

All CDKIs, identified so far, function by competing with ATP for binding to the catalytic site. The design of inhibitors specific to a particular protein kinase was originally thought of as an impossible task owing to the high degree of homology shared by the ATP binding domains of these enzymes. Actually, several CDKIs have entered clinical evaluation for the treatment of cancer. These include flavopiridol,[7] 7-hydroxystaurosporine (UCN-01),[8] roscovitine (CYC202),[9] and the aminothiazole compound (BMS-387032).[10] The identified CDKIs display antimitotic and apoptosis-inducing properties and are being evaluated as potential antitumor agents.[11] Furthermore, when used in combination with cytotoxic drugs, they can re-establish an otherwise deficient cell cycle checkpoint, which may enhance the activity of conventional treatments. Nowadays, the synthesis of novel highly selective CDKIs as candidates for CDK-target therapy in cancer treatment is in high demand.[12,13]

Computational models that are able to predict the biological activity of compounds by their structural

Keywords: Cyclin-dependent kinase inhibitors; QSAR analysis; 2D autocorrelation space; Bayesian-regularized genetic neural networks (BRGNN); CoMFA; CoMSIA.
* Corresponding author. Tel.: +56 71 201 662; fax: +56 71 201 561; e-mail addresses: jcaballero@utalca.cl; jmcr77@yahoo.com

0968-0896/$ - see front matter © 2008 Elsevier Ltd. All rights reserved.
doi:10.1016/j.bmc.2008.04.048

properties are powerful tools to design highly active molecules. In this sense, quantitative structure–activity relationship (QSAR) studies have been successfully applied for modeling biological activities of natural and synthetic chemicals.[14] QSAR studies have been carried out for modeling activities of several kinds of CDKIs. Some recent reports are cited thereafter: Pies et al.[15] employed multiple linear regression (MLR) analysis for establishing a QSAR model for the CDK1-inhibitory activity of a series of 22 9-substituted paullones. Samanta et al.[16] performed a QSAR study using MLR analysis for relating electrotopological and refractotopological state atom indexes, indicator parameters and atomic charges of 42 3-aminopyrazoles with their CDK2/cyclin A inhibitory potency. Fernández et al.[17] applied Bayesian-regularized genetic neural network (BRGNN) methodology for modeling the inhibitory activity of 98 1*H*-pyrazolo [3,4-*d*]pyrimidine derivatives against CDK4. In addition to the abovementioned works, some 3D-QSAR studies have been reported for CDKIs. The most widely used 3D-QSAR methodologies: CoMFA[18] (comparative molecular field analysis) and CoMSIA[19] (comparative molecular similarity indices analysis) consider the molecular interaction fields of the aligned molecules for the QSAR analysis. Several studies on 3D-QSAR for CDKIs are cited thereafter: Ducrot et al.[20] reported CoMFA and CoMSIA models for 93 purine derivatives as CDK1 inhibitors. Singh et al.[21] developed CoMFA models for indenopyrazole derivatives as CDK2 and CDK4 inhibitors with the intention of designing potential leads with a higher inhibitory and discriminatory activity against these enzymes. The same authors carried out CoMFA study on oxindole derivatives as CDK1 and CDK2 inhibitors.[22] Kunick et al.[23] developed CoMSIA models for the inhibition of CDK1, CDK5, and glycogen synthase kinase 3 (GSK3) by compounds from the paullone inhibitor family. Authors found that the differences in the electronic fields between their models can be taken into account for the further development of GSK3-selective paullones. A similar procedure was carried out by Dessalew et al.[24] These authors developed CoMFA models on bisarylmaleimide series as GSK3, CDK2 and CDK4 inhibitors with the intention of optimizing and enhancing the selectivity toward GSK3.

The current study involves the development of a set of 2D and 3D QSAR models to predict and interpret the CDK4/D inhibitory activity of a set of pyrido[2,3-*d*]pyrimidin-7-ones (PPOs) investigated by Barvian et al.[25] (the chemical structures are shown in Table 1). No previous QSAR model approach for the prediction of the activity of these compounds was located in the literature. The data set includes 60 compounds with the biological activity reported as IC_{50} values. The original study investigated the structure–activity trend of these molecules experimentally, but no computational models were developed. First, we established the structure–activity relationships with both MLR and Bayesian-regularized genetic neural network (BRGNN) approaches using 2D autocorrelation vectors.[26] Afterward, we attempted to obtain CoMFA and CoMSIA models. The outcome of the present work is a comprehensive qualitative and quantitative description of the molecular features of PPO derivatives relevant for a CDK4/D activity, which completes the picture of the structure–activity relationship of this class of compounds.

2. Results and discussion

2.1. 2D Autocorrelation approach

2.1.1. Linear modeling. In a first approach, MLR analysis combined with a linear genetic algorithm (GA) feature selection was performed on the training set (Table 1). We chose the best model as the most reliable linear relationship between the calculated 2D autocorrelation descriptors and the binding affinity $\log(10^6/IC_{50})$. The best linear model is shown in:

$$\begin{aligned}\log(10^6/IC_{50}) &= -88.014\times \mathrm{MATS1m} - 6.215\times \mathrm{MATS6e} \\ &\quad + 13.944\times \mathrm{MATS8e} - 5.836\times \mathrm{GATS1v} \\ &\quad - 1.991\times \mathrm{GATS8v} + 93.994 \\ N = 50,\ R^2 &= 0.734,\ S = 0.631,\ p < 10^{-5} \\ Q^2 &= 0.669,\ S_{CV} = 0.664\end{aligned} \tag{1}$$

where N is the number of compounds included in the training set, R^2 is the square of correlation coefficient, S is the standard deviation of the regression, p is the significance of the variables in the model, Q^2 and S_{CV} are the correlation coefficient and standard deviation of the leave-one-out (LOO) cross-validation, respectively.

The linear model in Eq. 5 is able to explain about 73.4% of CDK inhibitory activity variance. Since Q^2 value was about 0.669, the model was considered to be a good predictive one. The MLR training set predictions ($\log(10^6/IC_{50})$) for the PPOs against CDK4/D appear in Table 1. In turn, plots of training set and LOO cross-validation predictions versus experimental $\log(10^6/IC_{50})$ values are shown in Figure 1. MLR model includes three Moran's indices (MATS1m, MATS6e, and MATS8e) and two Geary's coefficients (GATS1v and GATS8v). It is noteworthy that there is no significant intercorrelation between these descriptors, as it is seen in Table 2. According to the MLR model, atomic mass and van der Waals volume weighted terms have a negative influence in the inhibition of CDK4/D; meanwhile, atomic Sanderson electronegativity weighted terms show a complex influence, and atomic polarizabilities did not show any effect.

2.1.2. BRGNN. Despite the agreeable results found by GA combined with MLR analysis, we carried out an additional nonlinear search for exploring other possibilities. Recently, we proposed the BRGNN approach[27] which surpassed the limits of the linear solutions when modeling of inhibitory activities was performed.[28–32] This can be ascribed to the facilities of ANNs for approximating complex relations by hyperbolic tangent transfer function employment. The assistance of Bayesian regularization brings stability and avoids overfitting effects when nonlinear GA search is developed. In our

Table 1. Experimental and predicted CDK4/D inhibitory activities of pyrido[2,3-*d*]pyrimidin-7-one (PPO) derivatives

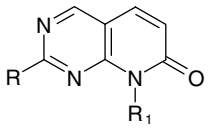

Compound	R	R_1	Exp.	MLR	BRGNN	CoMSIA
Training set						
1	NHPh	Et	3.21	3.02	2.75	2.78
2	NHEt	Et	1.92	2.17	1.42	1.90
3	NH *i*-Pr	Et	2.36	2.00	2.17	2.09
4	NH *t*-Bu	Et	2.28	1.94	2.88	2.01
5	NH cyclohexyl	Et	2.48	3.17	2.41	2.08
6	NHBn	Et	1.40	2.43	1.89	1.80
7	N(Me)Ph	Et	1.40	1.56	1.57	2.43
8	NH(3-F phenyl)	Et	2.85	2.23	2.40	2.40
9	NH(pyridin-4-yl)	Et	2.93	2.87	2.69	2.30
10	NHPh (3- OCF_2CHF_2)	Et	2.11	1.98	1.79	1.95
11	NHPh (3-OMe)	Et	1.40	1.28	1.84	1.64
12	NHPh(4-OMe)	Et	3.22	3.15	2.92	3.27
13	NHPh(4-OH)	Et	3.23	2.97	2.76	3.13
14	NH(3,4-diMeO phenyl)	Et	2.39	1.57	2.35	2.20
15	NHPh [4-$(O(CH_2)_2NEt_2)$]	Et	3.80	4.26	3.89	3.33
16	NHPh (NMe_2)	Et	3.48	3.64	3.53	3.15
17	NHPh [4-(1*H*-pyrrol-1-yl)]	Et	2.56	2.51	3.01	2.73
18	NHPh [4-(3-hydroxypropyl)piperidin-1-yl]	Et	3.05	4.20	4.22	3.33
19	NHPh [4-(4-methylpiperazin-1-yl)]	Et	4.07	4.01	4.18	3.50
20	NHPh	Me	2.26	2.55	2.52	2.56
21	NHPh	*n*-Propyl	3.26	3.19	3.19	3.35
22	NHPh	Sec-butyl	3.72	3.44	3.06	3.34
23	NHPh	*n*-Butyl	2.83	3.38	3.49	3.13
24	NHPh	Isobutyl	3.53	3.36	3.06	3.33
25	NHPh	Isopentyl	3.80	3.47	3.88	3.28
26	NHPh	Cyclopentyl	3.68	3.52	3.89	3.69
27	NHPh	Cyclohexyl	4.33	3.70	3.82	3.97
28	NHPh	Cycloheptyl	3.74	3.88	3.64	4.18
29	NHPh	Exo-1-bicyclo[2.2.1]hept-2-yl	4.42	3.85	4.22	3.85
30	NHPh	Phenyl	2.78	2.95	2.34	3.69
31	NHPh	Cyclohexylmethyl	1.87	2.67	2.40	3.05
32	NHPh	CH_2Ph	3.03	2.31	2.64	3.27
33	NHPh	Methoxymethyl	2.38	2.13	3.04	2.96
34	NHPh	2-Methoxyethyl	2.54	2.69	2.56	2.27
35	NHPh	*C*-Oxiranylmethyl	2.30	2.68	2.46	2.26
36	NHPh	CH_2CO_2Me	1.51	2.10	2.03	1.58
37	NHPh [4-$(O(CH_2)_2NEt_2)$]	Isopropyl	4.35	4.50	4.50	4.36
38	NHPh [4-$(O(CH_2)_2NEt_2)$]	Cyclopentyl	6.15	4.69	4.62	5.28
39	NHPh [4-$(O(CH_2)_2NEt_2)$]	Cyclohexyl	4.96	4.72	4.59	5.38
40	NHPh [4-$(O(CH_2)_2NEt_2)$]	Cycloheptyl	5.40	4.86	4.74	4.93
41	NHPh [4-$(O(CH_2)_2NEt_2)$]	Exo-1-bicyclo[2.2.1]hept-2-yl	3.35	4.87	4.37	3.82
42	NHPh [4-(4-methylpiperazin-1-yl)]	2-benzyloxyethyl	2.68	3.88	2.77	3.45
43	NHPh [4-(4-methylpiperazin-1-yl)]	$CH_2(CHOH)CH_2OH$	2.78	3.94	3.21	2.54
44	NHPh [4-(4-methylpiperazin-1-yl)]	Cyclopropyl	3.85	4.17	4.00	4.27
45	NHPh [4-(4-methylpiperazin-1-yl)]	Isopropyl	4.49	4.31	4.77	4.73
46	NHPh [4-(4-methylpiperazin-1-yl)]	Isopentyl	4.89	4.25	5.12	4.48
47	NHPh [4-(4-methylpiperazin-1-yl)]	Exo-1-bicyclo[2.2.1]hept-2-yl	5.22	4.55	5.21	4.98
48	NHPh [4-(4-methylpiperazin-1-yl)]	Cyclohexyl	5.40	4.45	4.93	5.56
49	NHPh [4-(3-hydroxypropyl)piperidin-1-yl]	Cyclopentyl	4.47	4.49	4.89	5.07
50	NHPh [4-(3-hydroxypropyl)piperidin-1-yl]	Exo-1-bicyclo[2.2.1]hept-2-yl	5.10	4.67	4.64	4.59
Test set						
51	NH(4-F phenyl)	Et	2.91	2.74	2.38	2.75
52	NH(3-MeO,4-OH phenyl)	Et	2.74	1.11	1.71	2.05
53	NHPh [4-$O(CH_2)_2OMe$]	Et	2.63	4.29	3.50	3.03
54	NHPh (NEt_2)	Et	2.85	1.83	2.84	3.12
55	NHPh[4-(morpholin-4-yl)]	Et	3.52	3.99	3.81	3.54
56	NHPh[piperidin-1-yl]	Et	3.52	3.22	3.59	3.59
57	NHPh	Isopropyl	3.84	3.47	3.21	3.20

(*continued on next page*)

Table 1 (*continued*)

Compound	R	R_1	Exp.	MLR	BRGNN	CoMSIA
58	NHPh	2-Ethoxyethyl	2.11	1.01	2.00	2.46
59	NHPh [4-(4-methylpiperazin-1-yl)]	Phenyl	3.76	3.85	3.65	5.00
60	NHPh [4-(4-methylpiperazin-1-yl)]	Cyclopentyl	5.05	4.40	4.59	5.33

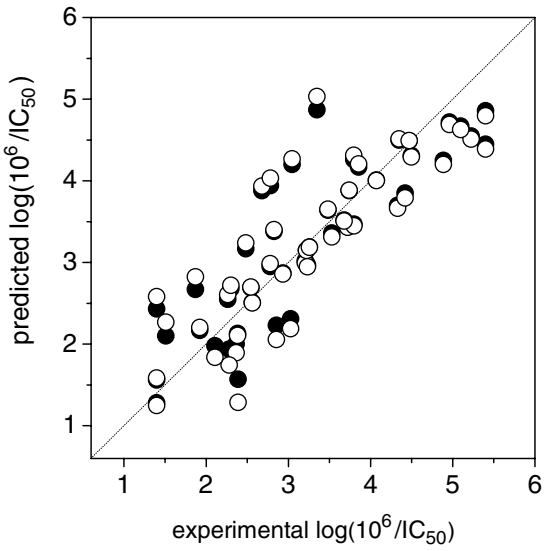

Figure 1. Plot of predicted versus experimental $\log(10^6/IC_{50})$ values for CDK4/D inhibition by pyrido[2,3-*d*]pyrimidin-7-one derivatives using MLR model. (●) Training set predictions; (○) LOO cross-validation predictions.

current application, ANN architectures were varied testing different quantities of neurons in hidden layers.

The descriptors and statistics of the best BRGNN model are depicted in Table 3 and plots of predicted versus experimental $\log(10^6/IC_{50})$ values are shown in Figure 2. The best BRGNN model includes five variables and contains two nodes in the hidden layer; furthermore, the architecture was quite stable since Bayesian regularization avoids overfitting. The number of optimum parameters yielded by the Bayesian regularization was 14. Model performance appears satisfactory, considering mainly the good quality of the internal validation parameter $Q^2 = 0.635$.

BRGNN model includes one Broto–Moreau's autocorrelation coefficient (ATS1m), two Moran's indices (MATS1m and MATS3e), and two Geary's coefficients (GATS4v and GATS8e). It is noteworthy that there is no significant intercorrelation between these descriptors, as it is seen in Table 2. In order to gain a deeper insight on the relative effects of each 2D autocorrelation descriptor in our model, a recently reported weight-based input ranking scheme was carried out. Black-box nature of three layers ANNs has been 'deciphered' in a recent report of Guha et al.[33] Their method allows understanding how an input descriptor is correlated to the predicted output by the network and consists of two parts: First, the nonlinear transform for a given neuron is linearized. Afterward, the magnitude in which a given neuron affects the downstream output is determined. Next, a ranking scheme for neurons in the hidden layer is developed. The ranking scheme is carried out by determining the square contribution values (SCV) for each hidden neuron (see Ref. 33 for details).

The results of ANN deciphering studies are displayed in Table 4. The reported effective weight matrix for our model shows that the first hidden neuron has the major contribution to the model with a SCV value 20-fold higher than the second hidden neuron. On this neuron, ATS1m has the highest impact equal to 1.099. On the other hand, the second hidden neuron exhibits a major contribution of MATS1m = −1.527, but the poor SCV value for this neuron indicates that the effects of the descriptors in this neuron have less importance for our model. From the analysis of the sign of the effective weights, we can also derive the approximate effect of the selected descriptors. According to the sign of the effective weights in the first neuron, atomic mass weighted terms ATS1m and MATS1m have positive influences in $\log(10^6/IC_{50})$; however, both descriptors have a negative influence in the second neuron. Particularly, MATS1m has a high negative contribution in the second neuron. As in the linear model, BRGNN model showed a negative influence of the atomic van der Waals weighted term (GATS4v), atomic Sanderson electronegativity weighted terms showed a complex influence (MATS3e has a negative influence and GATS8e has a

Table 2. Correlation matrix of the 2D autocorrelation descriptors selected by linear and nonlinear GA

	MATS1m	MATS6e	MATS8e	GATS1v	GATS8v	ATS1m	MATS3e	GATS4v	GATS8e
MATS1m	1								
MATS6e	0.021	1							
MATS8e	0.004	0.458	1						
GATS1v	0.498	0.031	0.160	1					
GATS8v	0.000	0.140	0.153	0.105	1				
ATS1m	0.283	0.083	0.003	0.126	0.228	1			
MATS3e	0.006	0.217	0.062	0.000	0.133	0.109	1		
GATS4v	0.000	0.214	0.418	0.126	0.000	0.080	0.008	1	
GATS8e	0.003	0.146	0.599	0.134	0.366	0.022	0.145	0.153	1

Table 3. Descriptors and statistics for BRGNN 2D autocorrelation model[a]

Model	Descriptors	Training set					LOO cross-validation	
		n	Num. Par.	Opt. Par.	R^2	*S*	Q^2	S_{CV}
BRGNN	ATS1m, MATS1m, MATS3e, GATS4v, GATS8e	50	15	14	0.826	0.484	0.635	0.695

[a] 5-2-1architecture was employed. Num. par. represents the number of neural network parameters; Opt. par. represents the optimum number of neural network parameters yielded by the Bayesian regularization.

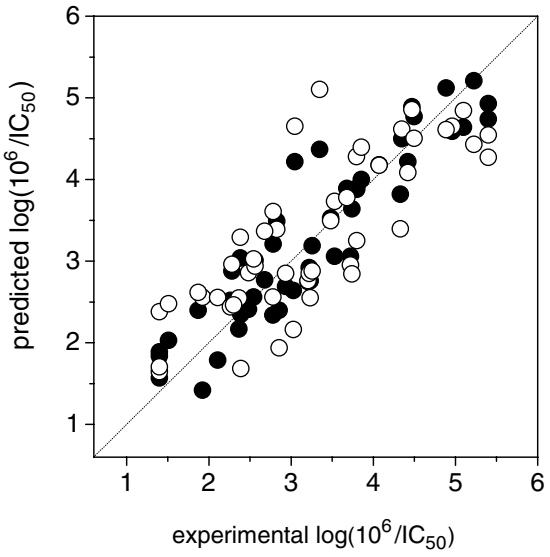

Figure 2. Plot of predicted versus experimental $\log(10^6/IC_{50})$ values for CDK4/D inhibition by pyrido[2,3-*d*]pyrimidin-7-one derivatives using BRGNN model. (●) Training set predictions; (○) LOO cross-validation predictions.

Table 4. Effective weight matrix for the optimum BRGNN model

Network inputs	Hidden neurons	
	1	2
ATS1m	**1.099**	−0.309
MATS1m	0.548	**−1.527**
MATS3e	−0.022	−0.717
GATS4v	−0.062	−0.683
GATS8e	0.068	−0.538
SCV	0.952	0.048

Most relevant descriptors appear in bold letter. The columns are ordered by the SCVs for the hidden neurons, shown in the last row.

positive influence in the first neuron), and atomic polarizabilities did not show any effect.

2.2. Kohonen self-organizing map

In order to achieve data differentiation, a Kohonen self-organizing map (SOM) with 10×10 neurons was mapped with GA-selected descriptors as input vectors. In a self-organizing neural network, if two input data vectors are similar, they will be mapped into the same neuron or into very close neurons in the 2D map. Therefore, either group in the map can be interpreted as a set of analogs defined by the vectorial space. Figure 3 depicts a Kohonen SOM for the 60 PPOs inhibitors collected in this work (training and test set). It is clearly visible that compounds are adequately distributed across the entire map: 48 of a total of 100 neurons were occupied. As it is observed, compounds with a similar range of activities were grouped into neighboring areas. It is noteworthy that there is a kind of gradient from the most active compounds at the upper left zone to the less active compounds at the lower right zone. As a consequence, this map can be used to carry out qualitative predictions. The position in the map would be able to assign an approximate range of activity for unknown compounds.

ANNs are generally more accurate predictors than other classes of models; however, they do not offer any information regarding how the inputs values correlate with the output value. Additionally, 2D autocorrelation descriptors are not so easy to interpret despite the exploration of an ample pool by BRGNN methodology allows finding relevant features that distinguish the details of important substructural differences. The lack of interpretability forces the use of QSAR models as purely predictive tools rather than as an aid in the understanding of structure property trends. Despite the unclear physicochemical sense of 2D autocorrelation descriptors, they encode structural features (s.f.), such as the presence of substituents, rings, and branching patterns. In this sense, we inspected the Kohonen SOM for establishing the main characteristics differentiated by our vectorial space (Fig. 3B). The s.f. grouped by Kohonen SOM were examined and related to the range of the variables for each compound. Each compound has six variables for such analysis: the dependent variable [$\log(10^6/IC_{50})$] and the five independent variables [ATS1m, MATS1m, MATS3e, GATS4v, and GATS8e]. The inspection of the values of these variables in each zone allows finding some rules.

The active upper left zone of the Kohonen SOM contains compounds with large substituents at position 4 of phenylamino group at position 2 and bulky substituents at position 8 of pyrido[2,3-*d*]pyrimidin-7-one scaffold (Fig. 3B). Such features are characterized by values of ATS1m > 36 and MATS1m < 0.933. Interestingly, ATS1m takes values below 33 for zones occupied by less active compounds. For compounds in the lower left zone of the SOM, MATS1m also takes values below 0.933. This zone groups compounds with aliphatic substituents at amino group at position 2 of pyrido[2,3-*d*]pyrimidin-7-one scaffold. It is noteworthy that zones at the right of the SOM are characterized by MATS1m values above 0.931. We can conclude that MATS1m identified the presence of unsubstituted phenylamino substituent.

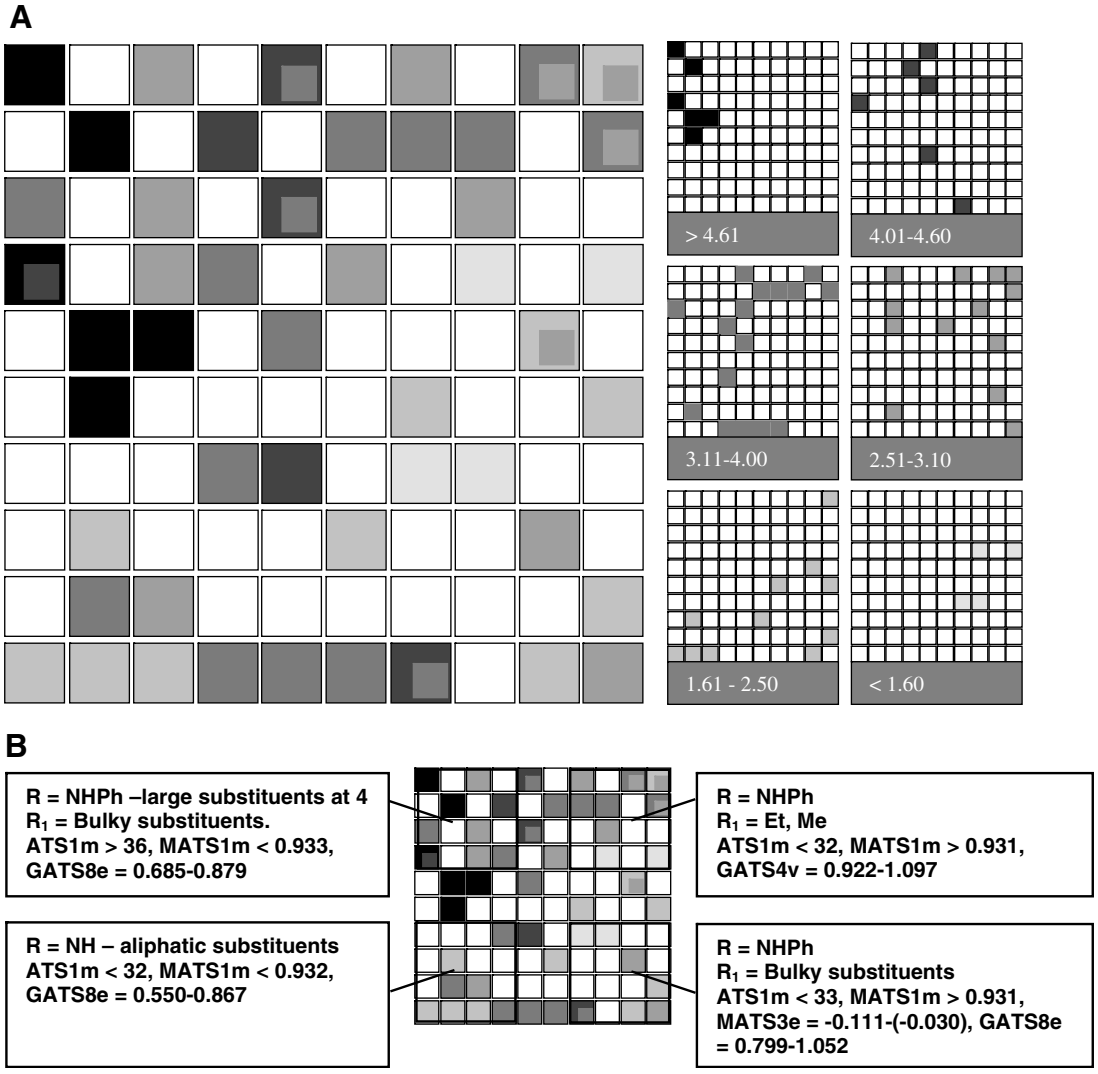

Figure 3. (A) Kohonen self-organizing map (SOM) for the data set using descriptors selected by nonlinear GA. Maps at right represent the ranges of pyrido[2,3-*d*]pyrimidin-7-one (PPO) activities [log(10^6/IC_{50})]. (B) Structural features (s.f.) differentiated by the Kohonen self-organizing map (SOM). Total range of descriptors: ATS1m = 20.0–45.6; MATS1m = 0.913–0.965; MATS3e = −0.213–0.277; GATS4v = 0.658–1.194; and GATS8e = 0.540–1.161.

According to ANN deciphering study (Table 4), ATS1m and MATS1m are the more important descriptors. Kohonen SOM also reveals that these descriptors identified the most general features which discriminate between active and inactive inhibitors. The remaining descriptors did not show significant differentiated behaviours in each zone. In general, MATS3e varies between −0.213 and 0.011. The only exception is compound **10** (MATS3e = 0.277), which contains the pentafluoroethoxy substituent on the phenylamino at position 2 of pyrido[2,3-*d*]pyrimidin-7-one scaffold. On the other hand, GATS4v varies between 0.658 and 1.194. Upper right zone has compounds with unsubstituted phenylamino group at position 2 and small substituents (Et or Me) at position 8 of pyrido[2,3-*d*]pyrimidin-7-one scaffold. GATS4v has high values for this zone (between 0.922 and 1.097). Finally, GATS8e varies between 0.540 and 1.161. Higher values of GATS8e are located at lower left zone according to averaged GATS8e values in each zone (Fig. 3B). This zone contains compounds with unsubstituted phenylamino group at position 2 and bulky substituents at position 8 of pyrido[2,3-*d*]pyrimidin-7-one scaffold.

2.3. CoMFA and CoMSIA results

In addition to 2D autocorrelation models, CoMFA and CoMSIA models were carried out to predict and interpret the PPO biological activities. Figure 4 shows the aligned molecules within the grid box (grid spacing 2.0 Å) used to generate the CoMFA and CoMSIA columns. The stepwise development of CoMFA and CoMSIA models using different fields[34,35] is presented in Table 5. The predictability of the models is the most important criterion for assessment of both methods. The best CoMFA model describing CDK4/D inhibition used both steric and electrostatic fields and has a Q^2 value of 0.605 using 9 components. In comparison to CoMFA, CoMSIA methodology has the advantage of exploring more fields. A more statistically robust model

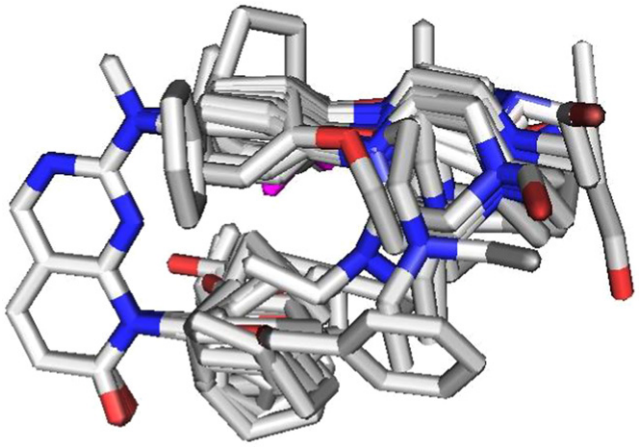

Figure 4. Atom-by-atom superposition used for 3D-QSAR analysis.

was obtained from the CoMSIA study. The best CoMSIA model included electrostatic and hydrophobic fields (CoMSIA-EH) and has a Q^2 value of 0.647 using only 2 components. CoMSIA-EH model showed an even contribution of both electrostatic and hydrophobic fields, explains 84.3 of the variance, has a low standard deviation ($s = 0.469$) and a high Fischer ratio ($F = 126.20$). CoMSIA models which only include only one field showed less reliable statistics, and the addition of other fields does not produce an improvement in the internal validation. The predictions of $\log(10^6/IC_{50})$ values for the 50 SSPs in the training set using CoMSIA-EH model are shown in Table 1. The correlations between the calculated and experimental values of $\log(10^6/IC_{50})$ (from training and LOO cross-validation) are shown in Figure 5.

The contour plots of the CoMSIA electrostatic and hydrophobic fields (stedv*coeff) are presented in Figure 6. For simplicity, the interaction between only the most active compound and the contour map is shown. Contour plots show the requirements of the basic scaffold of the pyrido[2,3-*d*]pyrimidin-7-one heterocycle for increasing CDK4/D inhibitory activity. The red/blue polyhedra denote regions in which negative/positive electrostatic potential is preferred for enhanced inhibitory activity; meanwhile, the yellow/white polyhedra denote regions in which hydrophobic/hydrophilic group is favorable for the activity. The plot shows a hydrophobic region (yellow isopleth) which extends from substituents at position 8 to substituents at position 2 of the pyrido[2,3-*d*]pyrimidin-7-one scaffold. This feature indicates that bulky hydrophobic substituents are required at both positions. These hydrophobic substituents are surrounded by white and blue polyhedra. The white regions at the end of substituents at position 2 indicate that hydrophilic atoms in this zone favor the inhibitory activity. The blue regions around substituents at position 2 indicate that there is an enhancement of the CDK4/D inhibition by increasing the positive charge at the end of this group. Better active molecules have NEt_2 or piperazine groups in this zone. A positive charge may arise due to the likelihood of the nitrogen getting charged under physiological conditions and hence increasing the positive charge. Finally, the red polyhedron indicates that negatively charged oxygen or nitrogen atoms at position 4 of the aromatic ring on position 2 of the pyrido[2,3-*d*]pyrimidin-7-one scaffold favor the CDK4/D inhibitory activity.

Trumpp-Kallmeyer et al.[36] performed 3D models of several pyrido[2,3-*d*]pyrimidin-7-one derivatives docked into the model of the ATP binding site of c-Src tyrosine kinase for identifying the binding mode of these inhibitors. Authors used X-ray structural information obtained from protein kinases with bound ATP and competitive inhibitors. As a result, authors found that these compounds bind in different orientation with respect to ATP. We analyzed how our CoMSIA-EH model satisfies the features of these 3D models. Considering this orientation in CDK4, the NH group at position 2 of the pyrido[2,3-*d*]pyrimidin-7-one may form a hydrogen bond to the carbonyl of Val-96 in CDK4, while the pyrimidine N3 nitrogen could form a hydrogen bond to the NH of the same residue. The hydrophobic substituents can be located at the entrance of the ATP binding pocket forming additional hydrophobic interactions with the peptide backbone and amino acid side chains (Ile-12, Val-20, Leu-147, and Ala-157) of the

Table 5. Results of the CoMFA and CoMSIA PLS analyses for CDK4/D inhibitors using several different field combinations

Model	NC	R^2	S	F	Q^2	S_{CV}	Fraction				
							Steric	Electrostatic	Hydrophobic	H-bond donor	H-bond acceptor
CoMFA-S	5	0.946	0.286	152.69	0.578	0.795	1				
CoMFA-E	2	0.701	0.647	55.11	0.351	0.954		1			
CoMFA-SE	9	0.994	0.099	743.21	0.605	0.746	0.566	0.434			
CoMSIA-S	5	0.897	0.392	76.96	0.578	0.794	1				
CoMSIA-E	2	0.739	0.605	66.44	0.500	0.837		1			
CoMSIA-H	1	0.691	0.651	107.28	0.569	0.769			1		
CoMSIA-D	3	0.141	1.109	2.52	0.000	1.201				1	
CoMSIA-A	2	0.299	0.991	10.03	0.140	1.098					1
CoMSIA-SE	4	0.921	0.340	130.83	0.625	0.741	0.374	0.626			
CoMSIA-SEH	2	0.839	0.475	122.64	0.634	0.716	0.236	0.363	0.401		
CoMSIA-EH	**2**	**0.843**	**0.469**	**126.20**	**0.647**	**0.704**		**0.480**	**0.520**		
CoMSIA-ALL	2	0.856	0.449	139.88	0.633	0.717	0.200	0.300	0.315	0.060	0.125

NC is the number of components from PLS analysis; R^2 is the square of the correlation coefficient; S is the standard deviation of the regression; F is the Fischer ratio; and Q^2 and S_{cv} are the correlation coefficient and standard deviation of the leave-one-out (LOO) cross-validation, respectively. The best model is indicated in boldface.

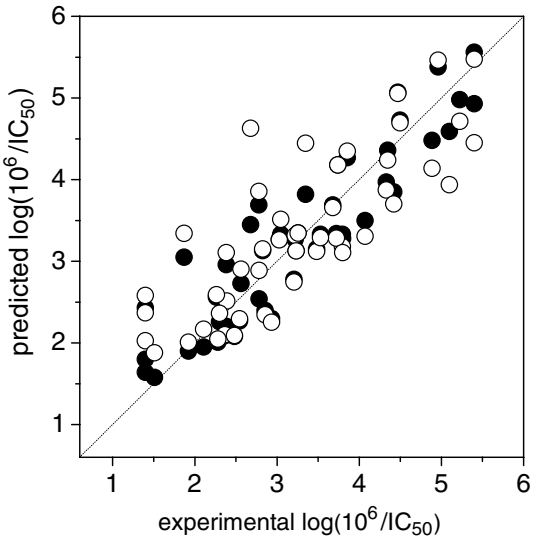

Figure 5. Plot of predicted versus experimental $\log(10^6/IC_{50})$ values for CDK4/D inhibition by pyrido[2,3-*d*]pyrimidin-7-one derivatives using CoMSIA-EH model. (●) Training set predictions; (○) LOO cross-validation predictions.

extended coil stretch, as is reflected by our CoMSIA-EH model. Furthermore, distal substituents off the 2-amino group can extend out of the binding pocket and can establish some interactions with some hydrophilic residues like Asp-99 and Glu-144. In our CoMSIA-EH model it is reflected by white and blue isopleths (hydrophilic and positively charged groups enhance the activity) at the end of the chain.

2.4. Test set predictions

High values of Q^2 are a necessary, but not a sufficient, condition for a model to possess significant predictive power. For a stronger evaluation of model applicability for prediction on new chemicals, the external validation of the models is also recommended.[37] We used 2D autocorrelation and CoMSIA-EH models to predict the inhibitory activities of an external test set of CDK4/D inhibitors that were not used in the training process. The results of the predictions are shown in Table 1. The plots of the predicted versus experimental values and the residuals are showed in Figure 7. This analysis reveals that all the models have acceptable predictive capacities. In general, the BRGNN procedure improves the linear results for 2D autocorrelation method according to regression. The increment in the quality of the prediction of the external test set is showy, from $R^2 = 0.477$ (R^2 of test set fitting) for the MLR model to $R^2 = 0.659$ for the BRGNN one. The analysis of the residuals shows that the average of 2D autocorrelation BRGNN and CoMSIA-EH models leads to a more precise prediction; in this sense, it is possible to combine both models for predictive purposes.

2D autocorrelation methodology ignores the 3D structure of the molecules considered for QSAR analysis. Despite the lack of interpretability, 2D autocorrelation BRGNN model is amenable for predicting an external set. Compounds **54**, **58**, and **59** are better predicted by this model. On the other hand, CoMSIA-EH model is able to provide a detailed interpretation of the structure–activity relationships for the studied PPOs (R^2 of test set fitting = 0.719) as well as to predict the activity of new compounds. Inhibitory activities of compounds **51**, **52**, **53**, **55**, **56**, and **60** are better predicted using this model.

Since our models are able to predict compounds in the test set, they can be used for predicting the activity of new compounds. A main concern of investigators interested in chemical synthesis and biological evaluations is how they can use QSAR models for predicting new active compounds. A simple way to predict the activity of a new compound is by using linear Eq. 1. 2D autocorrelation properties of the new compound can be calculated by using Dragon software (http://www.disat.unimib.it/chm/). The use of BRGNN 2D autocorrelation model as a predictive tool requires the use of neural network

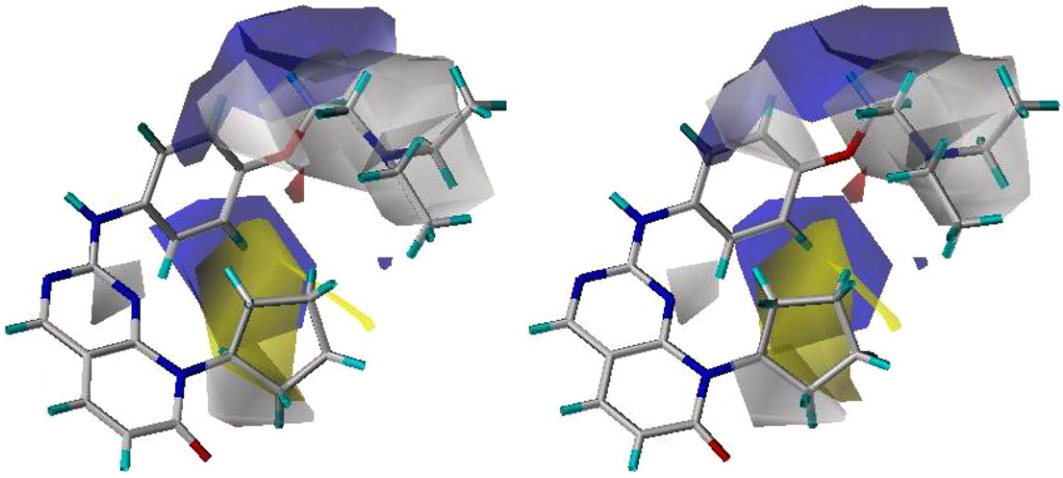

Figure 6. Stereoview of CoMSIA stdev*coeff contour map for CDK4/D inhibitors. Compound **38** is shown inside the field. Blue polyhedra indicate regions where an increase of positive charge will enhance the activity, red polyhedra indicate regions where more negative charges are favorable for activity. Yellow and white polyhedra indicate regions where hydrophobic or hydrophilic groups, respectively, will enhance the activity.

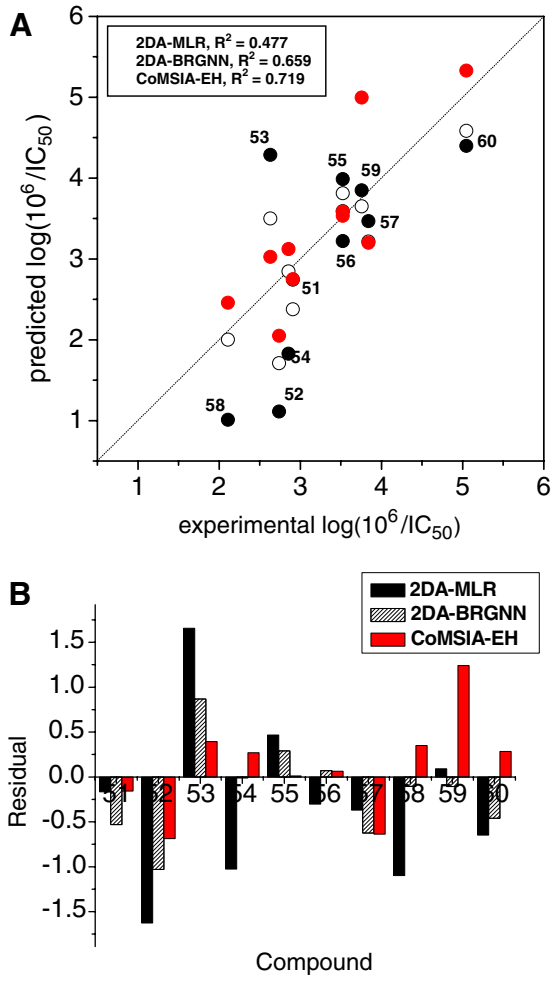

Figure 7. (A) Plot of predicted versus experimental $\log(10^6/IC_{50})$ values for test set compounds. (●) 2D autocorrelation MLR, (○) 2D autocorrelation BRGNN, and (●) CoMSIA-EH models. (B) Residuals for test set compounds.

and GA functions in MATLAB environment.[38] A simple way to evaluate the activity of a new compound is by training a Kohonen SOM with 2D autocorrelation vectors selected by nonlinear GA search for the 60 compounds used in this work, joined with the vectors of the new compound we want to predict, using the NNTool of MATLAB (www.mathworks.com/access/helpdesk/help/toolbox/nnet/nntool.html). The position of the new compound related to the compounds trained in this work indicates whether or not the new compound is active (2D autocorrelation vectors selected by nonlinear search for the 60 compounds in this report are included in Supplementary data). Finally, the use of CoMSIA-EH model as a predictive tool requires the use of Sybyl.[39] The user should reproduce our model and predict new compounds by aligning them in the same grid.

3. Conclusions

Predictive QSAR models were derived for pyrido[2,3-*d*]pyrimidin-7-one (PPO) derivatives as inhibitors of CDK4/D, which should be useful for assisting the design of active compounds. Such models correlate well structural features with inhibitory activities against CDK4/D and bring valuable information about the relevant characteristics of inhibitors.

First, 2D autocorrelation models were developed using MLR and Bayesian-regularized artificial neural networks (BRANNs) combined with GA feature selection (BRGNN method). 2D autocorrelation space was combined with different weighting schemes, viewed as an adaptive descriptor space, containing topological information able to capture structural complexity. The 2D autocorrelation descriptors appeared to capture sufficient structural detail to yield very useful results in modeling biological properties. Both linear and nonlinear methods bring statistically reliable results; however, BRGNN model is successful in predicting a set of compounds of an external set. Our results corroborate that the employment of 2D autocorrelation descriptors is extremely useful in QSAR studies giving simple correlations between the molecular structures and biological activities.

Afterwards, traditional CoMFA and CoMSIA approaches have been applied to derive the same relationships. A reliable model was obtained by using steric and electrostatic CoMFA fields; however, when using electrostatic and hydrophobic CoMSIA fields, a better statistically meaningful model was derived. Thus, prediction of CDK4/D activities with sufficient accuracy should be possible. Moreover, an interpretation of the CoMSIA fields makes it possible to draw conclusions concerning the most appropriate features for the analogues.

On the basis of the current results, the reported models have the potential to discover new potent inhibitors and bring useful molecular information about the ligand specificity for interacting with CDK4/D binding pocket.

4. Computational methods

4.1. Data sets: source and prior preparation

Inhibitions of CDK4/D for 60 PPOs were taken from the literature.[25] For modeling, IC_{50} activities were converted in logarithmic activities $\log(10^6/IC_{50})$, where 10^6 guarantees that logarithmic activities range between 1 and 9. The chemical structures and experimental activities ($\log(10^6/IC_{50})$) are shown in Table 1. The activity parameters IC_{50} (μM) are measures of inhibitory activity and refer to the nanomolar concentration of the compounds leading to 50% inhibition of the CDK. Prior to molecular descriptor calculations, 3D structures of the studied compounds were geometrically optimized using the semiempirical quantum-chemical method PM3[40] implemented in the MOPAC 6.0 computer software.[41] The data set was divided in training and test sets. Ten compounds were chosen randomly as a test set and were used for external validation for the MLR, BRGNN, CoMFA, and CoMSIA models. The compounds in the test sets were reserved to validate poten-

tial models. For the development of the models, the training sets included all the 50 remaining compounds.

4.2. 2D Autocorrelation pool

Three spatial autocorrelation vectors were employed for modeling the inhibitory activity: Broto-Moreau's autocorrelation coefficients (*ATS*) (Eq. 2),[42] Moran's indices (*MATS*) (Eq. 3),[43] and Geary's coefficients (*GATS*) (Eq. 4).[44]

$$\mathrm{ATS}(p_k, l) = \sum\nolimits_i \delta_{ij} p_{ki} p_{kj} \tag{2}$$

$$\mathrm{MATS}(p_k, l) = \frac{N}{2L} \frac{\sum_{ij} \delta_{ij} (p_{ki} - \bar{p}_k)(p_{kj} - \bar{p}_k)}{\sum_i (p_{ki} - \bar{p}_k)} \tag{3}$$

$$\mathrm{GATS}(p_k, l) = \frac{N-1}{4L} \frac{\sum_{ij} \delta_{ij} (p_{ki} - \bar{p}_k)(p_{kj} - \bar{p}_k)}{\sum_i (p_{ki} - \bar{p}_k)} \tag{4}$$

where ATS (p_k,l), MATS (p_k,l), and GATS (p_k,l) are Broto-Moreau's autocorrelation coefficient, Moran's index, and Geary's coefficient at spatial lag l, respectively; p_{ki} and p_{kj} are the values of property k of atoms i and j, respectively; is the average value of property k, L is the number of nonzero values in the sum, N is the number of atoms in the molecule, and $\delta(l,d_{ij})$ is a Dirac-delta function defined as

$$\delta(l, d_{ij}) = \left\{ \begin{array}{lll} 1 & \text{if} & d_{ij} = l \\ 0 & \text{if} & d_{ij} \neq l \end{array} \right\} \tag{5}$$

where d_{ij} is the topological distance or spatial lag between atoms i and j.

Spatial autocorrelation measures the level of interdependence between properties, and the nature and strength of that interdependence. In a molecule, Moran's and Geary's spatial autocorrelation analysis tests whether the value of an atomic property at one atom in the molecular structure is independent of the values of the property at neighboring atoms. If dependence exists, the property is said to exhibit spatial autocorrelation. The autocorrelation vectors represent the degree of similarity between molecules. The Dragon software[45] was used for calculating weighted Broto-Moreau, Moran and Geary 2D-autocorrelation vectors. Four different weighting schemes have been used: atomic masses (m), atomic van der Waals volumes (v), atomic Sanderson electronegativities (e), and atomic polarizabilities (p). Autocorrelation vectors were calculated at spatial lags l ranging from 1 up to 8. The autocorrelation descriptors are denoted by the scheme: type of descriptor-spatial lag-weighting property; for instance, GATS6v is the Geary autocorrelation of lag 6 weighted by atomic van der Waals volumes.

A data matrix was generated with the spatial autocorrelation vectors calculated for each compound. Afterwards, dimensionality reduction methods were employed for selecting the most relevant vector components for building MLR and BRGNN models. The total number of computed descriptors was 96. Descriptors with constant values were discarded. For the remaining descriptors, pairwise correlation analysis was performed in order to reduce, in a first step, the colinearity and correlation between descriptors. The procedure consists on the elimination of the descriptor with lower variance from each pair of descriptors with the modulus of the pair correlation coefficients higher than a predefined value ($R^2_{\max} = 0.95$). Afterwards, the number of remained descriptors was 41.

4.3. 2D Autocorrelation modeling procedure

Since many molecular descriptors were available for QSAR analysis and only a reduced subset of them is statistically significant in terms of correlation with biological activities, deriving an optimal QSAR model through variable selection needs to be addressed. Following the Occam's Razor,[46] we selected just the variables that contain the information that is necessary for the modeling but nothing more. In this sense, linear and nonlinear GA searches have been carried out in order to build the linear and nonlinear models.

4.3.1. Linear GA search. Linear GA search was carried out exploring MLR models. The mean square error of data fitting was tried as the individual fitness function. An initial population of 50 individuals was randomly extracted from the data matrix in the first generation. The succeeding generations were generated by crossover and single-point mutation operators, while the two best scoring individuals were automatically retained as members for the next round of evolution. The GA search ended when 90% of the generations showed the same target fitness score. Linear GA was programmed within the MATLAB environment using the genetic algorithm toolbox.[38] The best models were selected according to R^2 value ($R^2 > 0.8$) and the results of cross-validation experiments (higher Q^2).

4.3.2. Bayesian-regularized genetic neural networks (BRGNN). BRGNN is a framework that combines BRANNs with GA feature selection.[27,47] Our BRGNN approach is a version of the So and Karplus GA feature selection method[48] incorporating Bayesian regularization.

Bayesian networks are optimal devices for solving learning problems. They diminish the inherent complexity of artificial neural networks (ANNs) when complex models are automatically self-penalizing under Bayes' rule. The Bayesian approach to ANN modeling considers all possible values of network parameters weighted by the probability of each set of weights.[49,50] Bayesian approach yields a posterior distribution of network parameters $P(w|D,H)$ from a prior probability distribution $P(w|H)$ according to updates provided by the training set D using the BRANN model H. Predictions are expressed in terms of expectations with respect to this posterior distribution. Bayesian methods can simultaneously optimize the regularization constants in ANNs, a process that is very laborious using cross validation. Instead of trying to find the global minimum, the Bayesian approach finds the (locally) most probable parameters (see in more detail in Ref. 47).

BRANNs are accurate predictors for QSAR analysis.[51] They give models which are relatively independent of

ANN architecture, above a minimum architecture, since the Bayesian regularization method estimates the number of effective parameters. The concerns about overfitting and overtraining are also eliminated by this method so that the production of a definitive and reproducible model is attained. The joining of BRANN and GA feature selection (BRGNN) increases the possibilities of BRANNs for QSAR modeling as we indicated in previous works.[17,27–32,47]

Fully connected, three-layer BRANNs with back-propagation training were implemented in the MATLAB environment.[38] In these nets, the transfer functions of input and output layers were linear and the hidden layer had neurons with a hyperbolic tangent transfer function. Inputs and targets took the values from independent variables selected by the GA and $\log(10^6/IC_{50})$ values, respectively; both were normalized prior to network training. BRANN training was carried out according to the Levenberg–Marquardt optimization.[52] The initial value for μ was 0.005 with decrease and increase factors of 0.1 and 10, respectively. The training was stopped when μ became larger than 10^{10}.

The GA implemented in this paper keeps the same characteristics of the previously reported one in earlier work.[27] Initially, a set of 50 chromosomes were randomly generated. The population fitness was then calculated and the members were rank ordered according to fitness. The 2 best scoring models were automatically retained as members for the next round of evolution. More progeny models were then created for the next generation by preferentially mating parent models with higher scores. Crossover operator and single-point mutations were used in the evolution process until a 90% of the generations showed the same target fitness score. Our GA was programmed within the MATLAB environment using the genetic algorithm and neural networks toolboxes.[38] The predictors are BRANNs with a simple architecture (two or three neurons in a sole hidden layer). We tried the mean square error of data fitting for BRANN models, as the case may be, as the individual fitness function. The best models were selected according to R^2 value ($R^2 > 0.8$) and the results of cross-validation experiments (higher Q^2).

4.4. Kohonen self-organizing maps (SOMs)

The high predictive ability and flexibility of ANNs have made them very attractive to QSAR modelers. However, the lack of interpretability has led to the general characterization of ANN models as 'black boxes'. In previous work, we proposed the use of Kohonen SOMs for analyzing the meaning of the descriptors selected by BRGNN methodology according to the structural feature they encode.[31]

The Kohonen SOMs[53] are ANNs related to classic clustering algorithms, in that they generate groupings of data points taken to be described by a single vector of typical values. However, the SOMs are distinct from standard clustering methods in that they do not operate with separate clusters: rather, they allocate data points to groups which are related.[54]

Kohonen SOMs are networks of spatially related nodes each of which represents a 'prototype' of a particular region of data (input) space. Each node comprises a set of weights corresponding to the dimensions of the data. Their characteristic feature is their ability to map nonlinear relations in multidimensional data sets into easily visualizable 2D grids of neurons displaying the topology of a data set. Essentially, SOMs permit the perception of similarities in objects.

To settle structural similarities among the modeled CDKIs, a Kohonen SOM was built. The 2D autocorrelation descriptors selected by BRGNN methodology were used for unsupervised training of 10×10 neuron maps. SOMs were implemented in the MATLAB environment.[38] Neurons were initially located in a grid topology. The ordering phase was developed in 1000 steps with a 0.9 learning rate until a tuning neighborhood distance (1.0) was achieved. The tuning-phase learning rate was 0.02. Training was performed for a period of 2000 epochs in an unsupervised manner.

4.5. CoMFA and CoMSIA models

CoMFA and CoMSIA models were performed using the Sybyl 7.2 software of Tripos.[39] All the molecules were aligned by an atom-by-atom least-square fit. We used the pyrido[2,3-*d*]pyrimidin-7(8*H*)-one scaffold of the active compound **38** in its optimized conformation as a template. For the 3D-QSAR calculations previous data set splitting was kept. The molecules of the training set were placed in a rectangular grid extending beyond 4 Å in each direction from the coordinates of each molecule. The interaction energies between a probe atom (a sp^3 hybridized carbon atom with +1 charge) and all compounds were computed at the surrounding points, using a volume-dependent lattice with 2.0 Å grid spacing. Then, standard Sybyl parameters were used for a partial least squares (PLS) analysis. The number of components in the PLS models was optimized by using Q^2 value, obtained from the leave-one-out (LOO) cross-validation procedure, with the SAMPLS[55] sampling method. The number of components was increased until additional components did not increase Q^2 by at least 5% per added component. The CoMFA models were generated by using steric and electrostatic probes with standard 30 kcal/mol cutoffs. In the CoMSIA analyses, similarity is expressed in terms of steric occupancy, electrostatic interactions, local hydrophobicity, and H-bond donor and acceptor properties, using a 0.3 attenuation factor.

4.6. Analysis of the quality of the models

The quality of the fit of the training set of a specific model was measured by its R^2. However, a most important measure is the prediction quality. An internal LOO cross-validation process was carried out by estimating R^2 of LOO cross-validation (Q^2) and standard deviation (S_{CV}). A data point was removed (left-out) from the

training set, and the model was refitted; the predicted value for that point is then compared to its actual value. This is repeated until each datum has been omitted once; the sum of squares of these deletion residuals can then be used to calculate Q^2. In addition, the predictive power of the model was also measured by an external validation process that consists in predicting the activity of unknown compounds forming the test set. In this case, the residuals of predictions were evaluated. Such criteria have been formulated as the requirements for a QSAR model to have highly predictive power.

Acknowledgements

This work was supported by Innova Chile (FDI, CORFO), Project 06CN12PAT-51. We express our thanks to 'Red Iberoamericana de Bioinformática' RIB from CYTED, for partial financial support.

Supplementary data

Supplementary data associated with this article can be found, in the online version (2D autocorrelation vectors selected by nonlinear genetic algorithm search for pyrido[2,3-*d*]pyrimidin-7-one derivatives.) Supplementary data associated with this article can be found, in the online version, at doi:10.1016/j.bmc.2008.04.048.

References and notes

1. Harper, J. W.; Adams, P. D. *Chem. Rev.* **2001**, *101*, 2511.
2. Mihara, M.; Shintani, S.; Kiyota, A.; Matsumura, T.; Wong, D. T. W. *Int. J. Oncol.* **2002**, *21*, 95.
3. Gitig, D. M.; Koff, A. *Mol. Biotechnol.* **2001**, *19*, 179.
4. Kamb, A.; Gruis, N. A.; Weaver-Feldhaus, J.; Liu, Q.; Harshman, K.; Tavtigian, S. V.; Stockert, E.; Day, R. S., III; Johnson, B. E.; Skolnik, M. H. *Science* **1994**, *264*, 436.
5. Knockaert, M.; Greengard, P.; Meijer, L. *Trends Pharmacol. Sci.* **2002**, *23*, 417.
6. Kong, N.; Fotouhi, N.; Wovkulich, P. M.; Roberts, J. *Drugs Future* **2003**, *28*, 881.
7. Senderowicz, A. M.; Headlee, D.; Stinson, S. F.; Lush, R. M.; Kalil, N.; Villalba, L.; Hill, K.; Steinberg, S. M.; Figg, W. D.; Tompkins, A.; Arbuck, S. G.; Sausville, E. A. *J. Clin. Oncol.* **1998**, *16*, 2986.
8. Fuse, E.; Kuwabara, T.; Sparreboom, A.; Sausville, E. A.; Figg, W. D. *J. Clin. Pharmacol.* **2005**, *45*, 394.
9. Meijer, L.; Borgne, A.; Mulner, O.; Chong, J. P. J.; Blow, J. J.; Inagaki, N.; Inagaki, M.; Delcros, J. G.; Moulinoux, J. P. *Eur. J. Biochem.* **1997**, *243*, 527.
10. Misra, R. N.; Xiao, H.; Kim, K. S.; Lu, S.; Han, W.; Barbosa, S. A.; Hunt, J. T.; Rawlins, D. B.; Shan, W.; Ahmed, S. J.; Qian, L.; Chen, B.; Zhao, R.; Bednarz, M. S.; Kellar, K. A.; Mulheron, J. G.; Batorsky, R.; Roongta, U.; Kamath, A.; Marathe, P.; Ranadive, S. A.; Sack, J. S.; Tokarski, J. S.; Pavletich, N. P.; Lee, F. Y. F.; Webster, K. R.; Kimball, S. D. *J. Med. Chem.* **2004**, *47*, 1719.
11. Meijer, L.; Leclerc, S.; Leost, M. *Pharmacol. Ther.* **1999**, *82*, 279.
12. Arris, C. E.; Boyle, F. T.; Calvert, A. H.; Curtin, N. J.; Endicott, J. A.; Garman, E. F.; Gibson, A. E.; Golding, B. T.; Grant, S.; Griffin, R. J.; Jewsbury, P.; Johnson, L. N.; Lawrie, A. M.; Newell, D. R.; Noble, M. E. M.; Sausville, E. A.; Schultz, R.; Yu, W. *J. Med. Chem.* **2000**, *43*, 2797.
13. Wang, S.; Meades, C.; Wood, G.; Osnowski, A.; Anderson, S.; Yuill, R.; Thomas, M.; Mezna, M.; Jackson, W.; Midgley, C.; Griffiths, G.; Fleming, I.; Green, S.; McNae, I.; Wu, S.-Y.; McInnes, C.; Zheleva, D.; Walkinshaw, M. D.; Fischer, P. M. *J. Med. Chem.* **2004**, *47*, 1662.
14. Kubinyi, H. QSAR: Hansch analysis and related approaches. In *Methods and Principles in Medicinal Chemistry*; Mannhold, R., Krokgsgaard-Larsen, P., Timmerman, H., Eds.; VCH: Weinheim, 1993.
15. Pies, T.; Schaper, K.-J.; Leost, M.; Zaharevitz, D. W.; Gussio, R.; Meijer, L.; Kunick, C. *Arch. Pharm. (Weinheim, Ger.)* **2004**, *337*, 486.
16. Samanta, S.; Debnath, B.; Basu, A.; Gayen, S.; Srikanth, K.; Jha, T. *Eur. J. Med. Chem.* **2006**, *41*, 1190.
17. Fernández, M.; Tundidor-Camba, A.; Caballero, J. *J. Chem. Inf. Comput. Sci.* **2005**, *45*, 1884.
18. Cramer, R. D., III; Patterson, D. E.; Bunce, J. D. *J. Am. Chem. Soc.* **1988**, *110*, 5959.
19. Klebe, G.; Abraham, U.; Mietzner, T. *J. Med. Chem.* **1994**, *37*, 4130.
20. Ducrot, P.; Legraverend, M.; Grierson, D. S. *J. Med. Chem.* **2000**, *43*, 4098.
21. Singh, S. K.; Dessalew, N.; Bharatam, P. V. *Eur. J. Med. Chem.* **2006**, *41*, 1310.
22. Singh, S. K.; Dessalew, N.; Bharatam, P. V. *Med. Chem.* **2007**, *3*, 75.
23. Kunick, C.; Lauenroth, K.; Wieking, K.; Xie, X.; Schultz, C.; Gussio, R.; Zaharevitz, D.; Leost, M.; Meijer, L.; Weber, A.; Jørgensen, F. S.; Lemcke, T. *J. Med. Chem.* **2004**, *47*, 22.
24. Dessalew, N.; Bharatam, P. V. *Eur. J. Med. Chem.* **2007**, *42*, 1014.
25. Barvian, M.; Boschelli, D. H.; Cossrow, J.; Dobrusin, E.; Fattaey, A.; Fritsch, A.; Fry, D.; Harvey, P.; Keller, P.; Garrett, M.; La, F.; Leopold, W.; McNamara, D.; Quin, M.; Trumpp-Kallmeyer, S.; Toogood, P.; Wu, Z.; Zhang, E. *J. Med. Chem.* **2000**, *43*, 4606.
26. Fernández, M.; Tundidor-Camba, A.; Caballero, J. *Mol. Simul.* **2005**, *31*, 575.
27. Caballero, J.; Fernández, M. *J. Mol. Model.* **2006**, *12*, 168.
28. González, M. P.; Caballero, J.; Tundidor-Camba, A.; Helguera, A. M.; Fernández, M. *Bioorg. Med. Chem.* **2006**, *14*, 200.
29. Fernández, M.; Caballero, J. *Bioorg. Med. Chem.* **2006**, *14*, 280.
30. Fernández, M.; Caballero, J. *Chem. Biol. Drug Des.* **2006**, *68*, 201.
31. Fernández, M.; Caballero, J.; Tundidor-Camba, A. *Bioorg. Med. Chem.* **2006**, *14*, 4137.
32. Fernández, M.; Caballero, J. *Bioorg. Med. Chem.* **2007**, *15*, 6298.
33. Guha, R.; Stanton, D. T.; Jurs, P. C. *J. Chem. Inf. Model.* **2005**, *45*, 1109.
34. Caballero, J.; Saavedra, M.; Fernández, M.; González-Nilo, F. D. *J. Agric. Food Chem.* **2007**, *55*, 8101.
35. Caballero, J.; Fernández, M.; Saavedra, M.; González-Nilo, F. D. *Bioorg. Med. Chem.* **2008**, *16*, 810.
36. Trumpp-Kallmeyer, S.; Rubin, R. J.; Humblet, C.; Hamby, J.; Showalter, H. D. S. *J. Med. Chem.* **1998**, *41*, 1752.
37. Golbraikh, A.; Tropsha, A. *J. Mol. Graphics Modell.* **2002**, *20*, 269.
38. *MATLAB*, version 7.0; The Mathworks Inc.: Natick, MA. Available from: <http://www.mathworks.com>.
39. *SYBYL*, version 7.2; Tripos Inc.: 1699 South Hanley Rd., St. Louis, MO., 63144, USA.
40. Stewart, J. J. P. *J. Comput. Chem.* **1989**, *10*, 210.

41. *MOPAC*, version 6; U.S. Air Force Academy: Colorado Springs, CO.
42. Moreau, G.; Broto, P. *Nouv. J. Chim.* **1980**, *4*, 359.
43. Moran, P. A. P. *Biometrika* **1950**, *37*, 17.
44. Geary, R. F. *Incorp. Stat.* **1954**, *5*, 115.
45. Todeschini, R.; Consonni, V.; Pavan, M. *DRAGON*, version 2.1; Talete SRL: Milan, Italy.
46. Hawkins, D. M. *J. Chem. Inf. Comput. Sci.* **2004**, *44*, 1.
47. Fernández, M.; Caballero, J. *J. Mol. Graphics Modell.* **2006**, *25*, 410.
48. So, S.; Karplus, M. *J. Med. Chem.* **1996**, *39*, 1521.
49. Mackay, D. J. C. *Neural Comput.* **1992**, *4*, 415.
50. Mackay, D. J. C. *Neural Comput.* **1992**, *4*, 448.
51. Winkler, D. A.; Burden, F. R. *Biosilico* **2004**, *2*, 104.
52. Foresee, F. D.; Hagan, M. T. Gauss-Newton approximation to Bayesian learning. In: *Proceedings of the 1997 International Joint Conference on Neural Networks*, IEEE, Houston, 1997, pp. 1930–1935.
53. Kohonen, T. *Biol. Cybern.* **1982**, *43*, 59.
54. Mangiameli, P.; Chen, S. K.; West, D. *Eur. J. Oper. Res.* **1996**, *93*, 402.
55. Bush, B. L.; Nachbar, R. B., Jr. *J. Comput. Aided Mol. Des.* **1993**, *7*, 587.